The role of mass removal mechanisms in the onset of ns-laser induced plasma formation

D. Autrique,[1,2,a)] G. Clair,[3] D. L'Hermite,[4] V. Alexiades,[5] A. Bogaerts,[2] and B. Rethfeld[1]

[1]*Department of Physics and Optimas Research Center, TU Kaiserslautern, 67653 Kaiserslautern, Germany*
[2]*Department of Chemistry, University of Antwerp, 2610 Wilrijk, Belgium*
[3]*CEA, DAM, DIF, F-91297 Arpajon, France*
[4]*CEA, DEN, SEARS, LANIE, F-91191 Gif-sur-Yvette, France*
[5]*Department of Mathematics, University of Tennessee, 37996-1320 Knoxville, Tennessee, USA*

The present study focuses on the role of mass removal mechanisms in ns-laser ablation. A copper sample is placed in argon, initially set at standard pressure and temperature. Calculations are performed for a 6 ns laser pulse with a wavelength of 532 nm and laser fluences up to $10 \, \text{J/cm}^2$. The transient behavior in and above the copper target is described by a hydrodynamic model. Transmission profiles and ablation depths are compared with experimental results and similar trends are found. Our calculations reveal an interesting self-inhibiting mechanism: volumetric mass removal in the supercritical region triggers plasma shielding and therefore stops proceeding. This self-limiting process indicates that volumetric mass removal does not necessarily result in large ablation depths. © *2013 AIP Publishing LLC*. [http://dx.doi.org/10.1063/1.4812577]

I. INTRODUCTION

Pulsed ns-laser ablation has been investigated for many years. Despite the various analytical and material processing applications,[1–3] the technique is still under discussion. Laser ablation results in a cascade of tightly coupled processes which depend on the laser parameters, the material properties of the sample as well as on the ambient environment. During ns-laser irradiation the target material heats up, melts, evaporates, and finally expands into the ambient gas. Here, the laser pulse triggers breakdown, resulting in plasma that shields the target from the incoming laser light. Such back-coupling effects as well as the measurement conditions often complicate an experimental identification of the underlying mechanisms.

Contrary to experiments, theoretical models allow a separate study of the various processes and can therefore be considered as a complementary tool during the research quest. In the past decade, a large number of hydrocodes have been developed for the study of ns-pulsed laser ablation of metals.[4–16] Their popularity stems from the fact that they overcome the severe time- and length-scale limitations encountered in kinetic models.[17–23] Several hydrocodes suffer, however, from certain deficiencies on how they treat the target. Most models treat surface evaporation as the dominant mass removal mechanism.[4,6,8,10,12–16] It is characterized by a clear phase boundary between the liquid and vapor phases and a transient non-equilibrium layer adjacent to the boundary, known as the Knudsen layer.[24–26] In principle, these models only hold in a limited irradiance regime, typically $I < 1 \, \text{GW/m}^2$ for ns-pulses.[27,28] At higher intensities, the metal reaches the critical temperature, where the concept of a sharp phase boundary vanishes and the target treatment has to be revised.[9,11,27,28]

Various interesting strategies have been proposed to circumvent this issue. In several cases, the chosen laser regime[5,6,29,30] or plasma shielding[8,12,15] prevented the material from reaching its critical temperature. Note that during pulsed ns-laser irradiation, the material properties change significantly. As a consequence, the common assumption of constant thermophysical properties[8,10,12,13,15,16] becomes questionable. During laser heating the material heats up, expands, melts, and loses its ordered structure. Upon expansion, the electrical conductivity, thermal conductivity, reflectivity, and absorption coefficient decrease. In the vicinity of the critical point, the expanded metal behaves plasma-like, with free valence electrons strongly coupled to ions.[31] Here, screening of overlapping valence shells causes a metal-insulator transition. As a result, the electrical conductivity experiences a sudden drop.[31–34] Following the work of Batanov *et al.*,[32] certain authors treated the dielectric transition explicitly[35–37] and assumed a transparency front near $0.9 \, T_c$ propagating through the target. This idea is quite attractive from both a computational as well as a physical point of view, since one can still attach an evaporation front to the hot metal. Nevertheless, there are some important drawbacks here. First of all, a fixed temperature criterion for the dielectric transition does not exist and besides the layer should become *quasi-transparent*. As a result, the material can arrive in the supercritical region. Here, the concept of an evaporation front does not longer hold; the mass removal mechanism becomes volumetric and the modelling approach applied in Refs. 35–37 needs to be revised.

A macroscopic description of laser-material removal should treat the response of the material to variable pressure, energy, and density. Therefore, a multiphase approach

a)Electronic mail: dautriqu@physik.uni-kl.de

should be applied.[9,11] This implies that a hydrodynamic description of ns-laser ablation must account for the mechanisms *in* as well as *above* the target. As mentioned before, the various mechanisms are closely connected. Target dynamics will influence plume dynamics and vice versa. Hence, a hydrocode should account for target heating, surface and volumetric mass removal, as well as plume expansion and plasma formation.

This work mainly focuses on the initial stage of ns-laser ablation, since the distribution of the laser energy between the target and the plume drives all processes. A 1D-multiphase model is presented, that accounts for target as well as plume dynamics during pulsed ns-laser irradiation. A typical experimental situation encountered in chemical analysis setups, such as Laser Ablation Inductively Coupled Plasma Mass Spectrometry (LA-ICP-MS),[3] is modelled. Different mass removal mechanisms are distinguished and discussed. Results are shown for the material evolution near a copper surface. The copper target is immersed in argon, initially set at atmospheric pressure and room temperature. Calculations are performed for a 6 ns Nd-YAG laser pulse operating in the visible spectrum at 532 nm and laser fluences up to 10 J/cm^2.

II. MODEL

In modeling ns-laser irradiation, one can assume that the electron and lattice subsystems are in thermal equilibrium. Thus, target heating can be described by the usual heat conduction equation. Since the laser-heated material tends to achieve equilibrium with its ambient pressure, an internal energy formulation accounting for pressure relaxation in the solid or liquid state, is applied for the target description. Because material is removed from the target domain, laser heating can be described in a reference frame attached to the receding surface:

$$\frac{\partial U(x,t)}{\partial t} - v_{\text{rec}}(t)\frac{\partial U(x,t)}{\partial x} = \frac{\partial}{\partial x}\kappa(T)\frac{\partial T(x,t)}{\partial x} + S_{\text{las}}(x,t),$$
(1)

$$S_{\text{las}}(x,t) = (1-R(T))\alpha(T)I_a(t)e^{-\alpha(T)x},$$
(2)

$$\frac{\partial P_{\text{m}}(x,t)}{\partial t} - v_{\text{rec}}(t)\frac{\partial P_{\text{m}}(x,t)}{\partial x} = -\frac{(P_{\text{m}}(x,t)-P_{\text{amb}})}{\tau_{\text{mech}}(x)}.$$
(3)

The set of Eqs. (1)–(3) is solved in the half space $(0 \leq x < \infty)$. In Eq. (1), U, κ, v_{rec}, and S_{las} denote the internal energy density, the thermal conductivity, the recession velocity due to surface and volumetric mass removal, and the laser source term, respectively. The latter, given by Eq. (2), involves the reflectivity R, absorption coefficient α and the laser intensity arriving at the surface I_a. The temperature dependent thermal conductivity for copper is retrieved from Ref. 38. The optical properties R and α depend on the applied laser wavelength as well as on the temperature of the material. They are calculated by fitting the extended Drude model[39] to tabulated data[40] and applying the Wiedemann-Franz law.

Equation (3) governs the relaxation of the material pressure P_{m} towards the ambient pressure P_{amb}. The time scale needed for pressure relaxation can be estimated from the mechanical relaxation time $\tau_{\text{mech}} = x/c_{\text{snd}}$. Here, c_{snd} and x denote the local sound velocity and the spatial coordinate, respectively. The material pressure will mainly rise in the region heated by the laser. The minimum relaxation time, $\tau_{\text{mech,min}}$, can therefore be estimated as the ratio of the absorption length and the speed of sound. This lower limit, $\tau_{\text{mech,min}}$, can be regarded as the characteristic mechanical relaxation time. For metals, one finds, typically, $\tau_{\text{mech,min}} \cong 10$ ps.[41] The target material will expand or compress locally after pressure relaxation. The corresponding material velocity can be obtained from the continuity equation:

$$\frac{\partial \rho(x,t)}{\partial t} - v_{\text{rec}}(t)\frac{\partial \rho(x,t)}{\partial x} = -\frac{\partial}{\partial x}\rho(x,t)v(x,t).$$
(4)

Here, ρ and v represent the material density and velocity, respectively. As soon as material is removed from the target, it will expand above the target surface. Here, various absorption mechanisms trigger breakdown in the vapor and a plasma is formed. This expanding plasma is treated by a set of convection-diffusion equations that account for mass, momentum, and energy conservation.[42,43] The set of equations describing the target and the plasma is closed by a multiphase equation-of-state.

Equation of state data describing the solid, stable, and metastable liquid as well as the two-phase and gas regions,[44] are merged with an equation of state for the plasma. The latter is described in the ideal gas approximation, assuming Local Thermodynamic Equilibrium (LTE).[45] A projection of the resulting phase diagram in the temperature-density plane is depicted in Figure 1. Here, the material phases and their
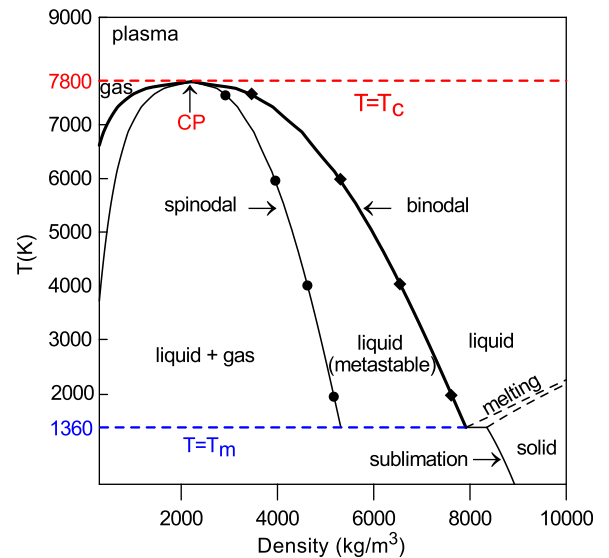

FIG. 1. Projection of phase diagram.[44] Four states of matter are shown: solid, liquid, gas and plasma, as well as the metastable liquid phase and the two phase region. The normal melting temperature ($T_{\text{m}} = 1360$ K), the critical temperature ($T_{\text{c}} = 7800$ K), and the critical point (CP) are indicated. The phase boundaries are represented by the melting and sublimation curves, binodal (thick line) and spinodal (thin line) and the two dashed lines at T_{m} and T_{c}, respectively. The liquid parts of the binodal (diamonds) and the spinodal (circles) are depicted.

respective phase boundaries are indicated. The onset of breakdown is modeled by a dimensionless collisional radiative model.[46,47] In a first step, the hydrodynamic model calculates the average internal energy and mass densities of the heavy species in the copper plume during the initial expansion stage. The latter information is then inserted in the collisional radiative code, where a set of rate equations describes the temporal evolution of the electron density and temperature, and the atomic level populations in the plume. These rate equations account for multiphoton ionization, electron impact excitation, and ionization, as well as the respective recombination reactions.[48] Finally, the collisional radiative model couples back to the hydrodynamic model: laser absorption coefficients for the related processes are calculated and inserted in the latter model. When the plume reaches a state close to LTE, the rate equations are switched off and the temperature, electron density, as well as the ion abundances are retrieved from the Saha equation.[45]

III. SURFACE MASS REMOVAL

When the surface temperature exceeds the normal boiling point of copper ($T_{\text{boil}} = 2836$ K), evaporation starts. During evaporation, copper atoms achieve translational equilibrium within a thin region close to the surface, known as the *Knudsen layer* (see Figure 2). There exists a variety of models describing the Knudsen layer at different scales and levels of detail.[20,24–26,49–54] One particular approach treats the Knudsen layer as a gas dynamic discontinuity.[24,25] Here, analytical expressions can be derived that interrelate temperature, pressure, density, and velocity along the target surface and the outer side of the Knudsen layer, respectively. In the present work, Knight's approach[25] is applied, since it treats evaporation in an ambient environment, in this case argon at 1 atm,

$$m = \frac{u_{\text{K}}}{\sqrt{2RT_{\text{K}}}}, \tag{5}$$

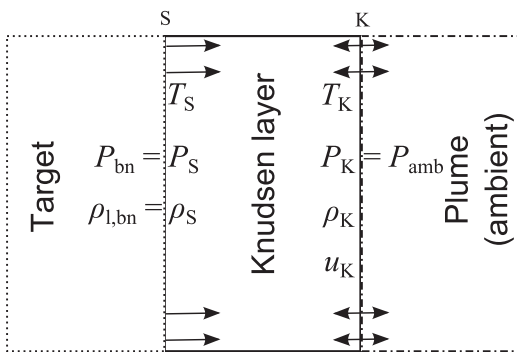$$M = m\sqrt{\frac{2}{\gamma}}, \tag{6}$$

FIG. 2. Schematic representation of Knudsen layer. The Knudsen layer (solid line) connects the target (dashed) and the ambient environment (dashed-dotted); here, the expanding copper plume. Properties at the surface (S) and at the end of the Knudsen layer (K) are indicated. The mass density, temperature, pressure, and velocity are denoted by ρ, T, P, and u, respectively. The properties at the surface are taken at the liquid part of the binodal (bn) (see also Fig. 1).

$$\frac{T_{\text{K}}}{T_{\text{S}}} = \left[\sqrt{1 + \pi\left(\frac{m}{2}\left(\frac{\gamma-1}{\gamma+1}\right)\right)^2} - \sqrt{\pi}\frac{m}{2}\left(\frac{\gamma-1}{\gamma+1}\right)\right]^2, \tag{7}$$

$$\frac{P_{\text{K}}}{P_{\text{S}}} = \sqrt{\frac{T_{\text{K}}}{T_{\text{S}}}}\left[\left(m^2 + \frac{1}{2}\right)e^{m^2}\text{erfc}(m) - \frac{m}{\sqrt{\pi}}\right]$$
$$+ \frac{1}{2}\left[1 - \sqrt{\pi}e^{m^2}\text{erfc}(m)\right] \quad \text{if } 0 \leq M \leq 1. \tag{8}$$

In Eqs. (5) and (6), R, γ, m, and M denote the specific gas constant, heat ratio, reduced Mach number, and Mach number of the particles, respectively. The mean velocity obtained by the atoms after several collisions is given by u_{K}. T_{K} and P_{K} are the temperature and pressure at the outer side of the Knudsen layer, whereas T_{S} and P_{S} denote the surface temperature and pressure. Note that the pressure ratio $P_{\text{K}}/P_{\text{S}}$, across the Knudsen layer governs the process type. As soon as the surface pressure P_{S} exceeds the ambient pressure P_{K}, evaporation starts and the Mach number becomes positive. This situation is described by Knight's relations (7, 8). During laser heating, however, the pressure at the outer side of the Knudsen layer can exceed the pressure at the target surface. As a result material starts to move towards the target; the phase transition reverses and condensation starts. Hence, the Mach number becomes negative and the pressure ratio exceeds unity ($P_{\text{K}}/P_{\text{S}} > 1$, $M < 0$). Contrary to evaporation, condensation can be subsonic, as well as supersonic.[52,55] In the supersonic case, all variables are extrapolated, whereas in the subsonic case the following pressure ratio is applied:[52,56]

$$\frac{P_{\text{K}}}{P_{\text{S}}} = 0.95e^{(2.42|M|)} \quad \text{if } M < 0. \tag{9}$$

The surface pressure P_{S} can be identified as the binodal pressure P_{bn} at the surface temperature T_{S}, whereas the pressure at the outer side of the Knudsen layer, P_{K}, can be regarded as the ambient plume pressure. Therefore, the pressure ratio becomes

$$\frac{P_{\text{K}}}{P_{\text{S}}} = \frac{P_{\text{amb}}}{P_{\text{S}}} = \frac{P_{\text{amb}}}{P_{\text{bn}}}. \tag{10}$$

As a result, the system of equations (1)–(9) can be properly closed. The following boundary conditions can now be defined for the plume domain:

$$F_\rho = \rho_{\text{K}}u_{\text{K}}, \tag{11}$$

$$F_{\rho u} = \rho_{\text{K}}u_{\text{K}}^2 + P_{\text{K}}, \tag{12}$$

$$F_{\rho e} = (\rho_{\text{K}}e_{\text{K}} + P_{\text{K}})u_{\text{K}} - Q_{\text{rad}}. \tag{13}$$

Equations (11)–(13) denote the mass, momentum, and energy fluxes that enter the plume domain. ρ_{K} and e_{K} are the mass density and the specific total energy at the outer side of the Knudsen layer, respectively. The radiation heat flux Q_{rad} from the plasma towards the target is estimated as follows:[57]

$$Q_{\text{rad}} = \frac{\Delta x_{\text{pl}}}{2}(S_{\text{ff}} + S_{\text{bf}}). \tag{14}$$

Here, S_{ff} and S_{bf} denote the energy sources due to free-free (Bremsstrahlung emission) and bound-free (photorecombination) transitions,[45] respectively, whereas Δx_{pl} denotes the size of the near-surface cell in the plume domain. Note that Eq. (14) presumes that 50% of the emitted light reaches the target surface.

Finally, the recession velocity of the liquid surface due to evaporation (+) or condensation (–) can be derived

$$v_{\text{rec,ev}} = \frac{\rho_K u_K}{\rho_{l,\text{bn}}}. \tag{15}$$

In the latter expression, $\rho_{l,\text{bn}}$ denotes the liquid density, taken at the binodal at surface temperature T_S.

IV. VOLUMETRIC MASS REMOVAL

A. Subcritical state

In addition to surface mass removal mechanisms, volumetric processes are considered as well. Since the present model does not exclude that the material arrives in the metastable liquid phase, bubble formation is accounted for (see Fig. 3). The corresponding homogeneous nucleation rate J_{nuc} is derived from the Volmer-Döring theory,[58]

$$J_{\text{nuc}}(T, \rho_1) = \sqrt{\frac{3\sigma(T, \rho_1)}{m\pi}} \frac{\rho_1}{m} e^{-\frac{W_{\text{cr}}(T,\rho_1)}{kT}} e^{-\tau_{\text{cr}}/t}, \tag{16}$$

$$W_{\text{cr}}(T, \rho_1) = \frac{4\pi}{3} R_{\text{cr}}^2 \sigma(T, \rho_1), \tag{17}$$

$$R_{\text{cr}}(T, \rho_1) = \frac{2\sigma(T, \rho_1)}{P_{\text{bub}}(T, \rho_1) - P_1(T, \rho_1)}. \tag{18}$$

W_{cr} denotes the work needed to create a nucleus of critical radius R_{cr} against a surface tension σ, see Eqs. (17) and (18). Here, m, ρ_1, P_1, and P_{bub} express the atomic mass, liquid density, liquid, and bubble pressures, respectively. The surface tension vanishes at the critical temperature T_c as well as on the spinodal. It is calculated from an extension of Eötvös rule[59,60]
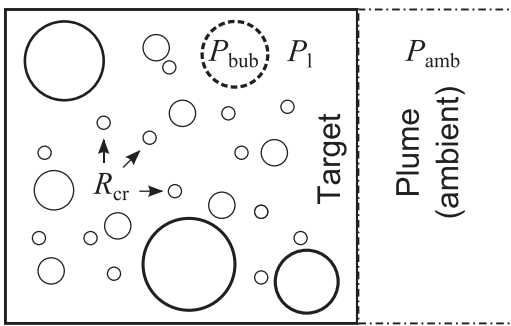

FIG. 3. Schematic representation of bubble formation in the subcritical state. Spherical nuclei with a critical radius R_{cr} are indicated. At any time, the liquid pressure P_1 will tend to adjust itself to the ambient pressure P_{amb}. Bubble growth is now controlled by the ratio of the pressures outside the bubble (liquid pressure P_1) and inside the bubble (bubble pressure P_{bub}). Since a hydrocode calculates physical properties that are spatially averaged over each computational cell, the model will provide average bubble sizes (dashed).

$$\sigma(T, \rho_1) = \sigma_{\text{m}} \frac{(T_c - T)}{(T_c - T_{\text{m}})} \left(\frac{\rho_{l,\text{bn}}(T) - \rho_{g,\text{bn}}(T)}{\rho_{l,\text{bn}}(T_{\text{m}}) - \rho_{g,\text{bn}}(T_{\text{m}})} \right)^{2/3}$$
$$\times \left(\frac{\rho_{l,\text{bn}}(T) - \rho_{l,\text{sp}}(T)}{\rho_1 - \rho_{l,\text{sp}}(T)} \right)^{1/2}. \tag{19}$$

In Eq. (19), $\rho_{l,\text{bn}}$, $\rho_{g,\text{bn}}$ denote the mass densities on the liquid and gas parts of the binodal, respectively, whereas the mass density on the liquid branch of the spinodal is given by $\rho_{l,\text{sp}}$. The melting and critical temperatures of copper are taken as $T_{\text{m}} = 1358\,\text{K}$ and $T_c = 7800\,\text{K}$, respectively. $\sigma_{\text{m}} = 1.29\,\text{J/m}^2$, is the surface tension of copper taken at the melting point.[61]

As soon as critical nuclei are formed, bubbles can grow. Bubble growth can be described by the Rayleigh equation:[58]

$$R(T, \rho_1) \frac{\partial^2 R(T, \rho_1)}{\partial t^2} + \frac{3}{2} \left(\frac{\partial R(T, \rho_1)}{\partial t} \right)^2$$
$$= \frac{1}{\rho_1} \left(P_{\text{bub}}(T, \rho_1) - P_1(T, \rho_1) - 2\frac{\sigma(T, \rho_1)}{R(T, \rho_1)} \right). \tag{20}$$

Bubble growth is governed by the pressure difference over the bubble $P_{\text{bub}} - P_1$ (see also Fig. 3). Hence when the pressure ratio $P_1/P_{\text{bub}} < 1$, bubbles grow; when $P_1/P_{\text{bub}} > 1$ they shrink and eventually collapse. Since the binodal pressure provides a reasonable estimate for the bubble pressure,[62] one can therefore take $P_{\text{bub}}(T, \rho_1) = P_{\text{bn}}(T)$. When a nucleus becomes smaller than the critical one, the released energy upon volume formation is not sufficient to create its surface and nucleation stops. The critical radius should therefore be regarded as a lower limit in the calculations. Note that Rayleigh's equation (20), reduces to the expression for the critical radius (18), under the assumption of mechanical equilibrium. The characteristic time τ_{cr} (see (16)), required to form a spherical bubble with critical volume $V_{\text{cr}} = 4\pi R_{\text{cr}}^3/3$, defines the onset time of bubble formation applied in the calculations. It can be estimated from Rayleigh's equation assuming radial growth from $R = 0$ to $R = R_{\text{cr}}$. Note that the characteristic time τ_{cr} depends strongly on the material properties and hence on the exact location of the material in the metastable region. We found for the applied laser settings, characteristic times τ_{cr} that varied between 10 ps and 1 ns, depending on the location in the metastable region. The latter characteristic time was found upon entrance in the metastable region, while the former onset times were calculated in the deepest observed locii in the metastable region.

The homogeneous nucleation rate (16), can therefore be interpreted as the rate at which a certain population of liquid is converted into critical nuclei after a time lag τ_{cr}. Finally, note that bubble formation consists of two stages, namely, nucleation (16) and growth (20). Assuming that every nucleus acquires a spherical volume V_{bub}, the average speed of the liquid-vapor interface of the bubbles, in a computational cell of size Δx, can be calculated as follows:

$$v_{\text{bub}}(T, \rho_1) = \frac{\rho_{v,\text{bn}}(T)}{\rho_1} J_{\text{nuc}}(T, \rho_1) V_{\text{bub}}(T, \rho_1) \Delta x. \tag{21}$$

As homogeneous nucleation proceeds and bubbles grow, the metastable liquid will transform into a two-phase mixture. The actual composition of this mixture can now be retrieved from the corresponding locus in the phase diagram, at any temperature $T < T_c$. The vapor fraction is given by

$$f_v(T, \rho_l) = \frac{\rho_l - \rho_{l,bn}(T)}{\rho_{v,bn}(T) - \rho_{l,bn}(T)}. \qquad (22)$$

Accordingly, the vapor fraction in a computational cell of size Δx, can be calculated. Here, kinetics and thermodynamics are interrelated through the following expression:

$$\Delta x_{bub} = f_v \Delta x = \int_{\Delta t_{bub}} v_{bub}(t)\, dt \approx \Delta t_{bub}\, v_{bub}(T, \rho_l). \qquad (23)$$

Here, Δt_{bub} denotes the time required to convert the metastable liquid contained in a cell of size Δx into a two-phase system. Since a hydrocode provides only spatially averaged physical properties, the present model cannot provide any information about the spatial distribution of the bubbles. Instead, it is assumed that the bubbles are homogeneously distributed over the cell volume. Therefore, the computational cells break up into a mixture of liquid and vapor, as soon as they reach the two-phase state. The vapor part is subsequently added to the plume domain, whereas the remaining liquid cell fractions are treated as ejected droplets. Here, the mass, momentum, and total energy density contained in the nucleated cell regions can be calculated from the simultaneous solution of Eqs. (1)–(4) and Eqs. (22) and (23), respectively. These variables are finally integrated over the nucleated cell regions Δx_{bub}, ensuring mass, momentum, and energy conservation between target and plume. Finally, the recession velocity of the liquid surface due to bubble formation becomes

$$v_{rec,bub} = \frac{\Delta x}{\Delta t_{bub}} \approx \frac{v_{bub}}{f_v} \quad \text{if} \quad T < T_c \quad \text{and} \quad \rho_{l,sp} \le \rho < \rho_{l,bn}. \qquad (24)$$

B. Supercritical state

When the material reaches the critical temperature T_c, the surface tension vanishes as the liquid-vapor interface disappears. Upon laser heating, the liquid metal will immediately proceed towards the supercritical state at $T > T_c$. The supercritical cells are added to the vapor domain and treated as a dense weakly ionized plasma. Since kinetic relations cannot be defined anymore, a pure hydrodynamic approach is applied. Mass, momentum, and total energy density are directly retrieved from Eqs. (1) to (4), whereas integral relations ensure again conservation. As soon as the target cells arrive in their supercritical state, the target surface should be repositioned. The latter observation results in a simple expression for the volumetric recession velocities in the supercritical region,

$$v_{rec,c} = \frac{\Delta x}{\Delta t} \quad \text{if} \quad T \ge T_c. \qquad (25)$$

As a result, three mass removal mechanisms and corresponding recession velocities can be identified: surface mass removal due to evaporation and condensation; $v_{rec,ev}$ (15), volumetric mass removal due to bubble formation; $v_{rec,bub}$ (24) and volumetric mass removal in the supercritical region; $v_{rec,c}$ (25).

The recession velocity $v_{rec}(t)$ in Eq. (1) can therefore be formulated as follows:

$$v_{rec}(t) = v_{rec,ev}(t) + v_{rec,bub}(t) + v_{rec,c}(t). \qquad (26)$$

V. ROLE OF PRESSURE

In Secs. III and IV, the pressure showed up in several equations. It should be stressed that the pressure plays a crucial role in the material evolution. Since the target material tends to adjust itself to the ambient pressure, P_{amb}, the latter will define the temporal evolution of the target in the phase diagram. Correspondingly, the actual location of the near-surface cells in the phase diagram will define the type of mass removal mechanism. This manifests itself as well in the pressure ratios encountered in the kinetic relations derived above. For instance, when a target surface cell follows the liquid part of the binodal, surface mass removal mechanisms are encountered. Here, the process type will be governed by the pressure ratio P_{amb}/P_S (10): when the surface pressure exceeds the ambient pressure, evaporation starts; otherwise, the phase transition reverses and material condenses on the surface. In case the material ends up in the metastable region, homogeneous nucleation takes place and bubbles can grow. Bubble growth is influenced by the pressure ratio P_l/P_{bub}; see also Eqs. (18)–(20). Since the material pressure P_l tends to adapt to the ambient pressure P_{amb}, bubble growth is indirectly affected by the ambient pressure, P_{amb}. Hence, as long as the ambient pressure does not exceed the bubble pressure, the material pressure will not exceed it either. In this situation, the pressure ratio P_l/P_{bub} is smaller than unity, bubbles will grow and the material could end up in its two-phase state. In the opposite situation, bubbles would shrink, finally collapse and the material would be driven out of the metastable region and arrive in the stable liquid phase.

In Sec. VI, results are shown for the behaviour of a copper target after pulsed ns-laser irradiation. The role of the various mass removal mechanisms is intensively discussed. The copper target is surrounded by argon, initially set at standard temperature and pressure (STP). Calculations are performed for a 6 ns Nd-YAG laser pulse operating at 532 nm and laser fluences up to 10 J/cm^2.

VI. RESULTS

The temporal path of the target surface cell in the copper sample is depicted in Fig. 4. Shortly after the beginning of the laser pulse, the surface temperature exceeds the normal boiling point ($T_{boil} = 2836$ K) and evaporation starts. The evaporated matter will push the ambient gas, here argon, away from the target (not shown). Now the ambient environment experienced by the surface consists of evaporated
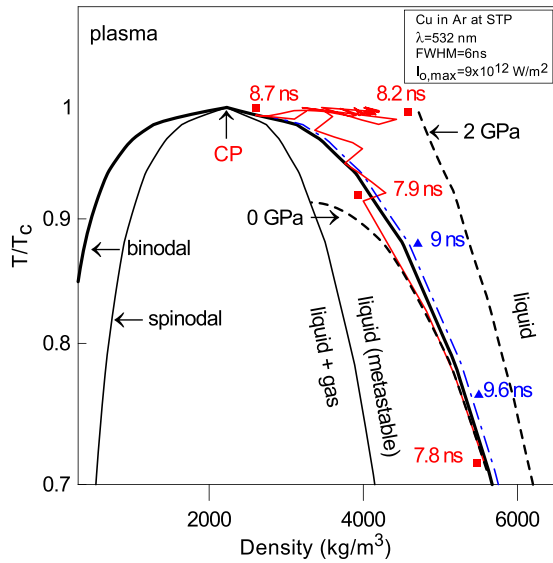
FIG. 4. Projection of phase diagram for temperatures between $0.7 T_c$ and T_c. The path of a surface cell is shown for 7.8–9.6 ns for the given conditions (box). Material heating (red squares) as well cooling (blue triangles) is observed. The two isobars (dashed) at 0 and 2 GPa, respectively, define the region of material evolution.

target material. Hence, P_{amb} can be regarded as the plume pressure close to the surface. Its minimum and maximum values will define the region of material evolution (see Sec. V). For the present fluence range (1–10 J/cm^2), isobars for the corresponding limits are shown in Fig. 4, i.e., $\min(P_{amb}) = 1$ atm $\cong 0$ GPa and $\max(P_{amb}) = 2$ GPa. After the onset of evaporation, the temperature of the target surface cell proceeds along the binodal line (red squares), up to approximately 7.8 ns, as shown in Figure 4. Evaporated material accumulates above the target and therefore the plume pressure above the target increases. Since a significant amount of laser energy is deposited in the copper target, the temperature and pressure inside the material increase. Since the material tends to relax towards the outer pressure, its density decreases. In a next stage, the material leaves the binodal and enters the metastable state. Here, it follows a path in the metastable region *close to the binodal*. Around 7.9 ns, a maximum deviation from the binodal is observed. At that instant, a minimum in the homogeneous nucleation time was found, here $\tau_{cr} \cong 30$ ps. Hence, bubble formation starts almost instantaneously, material is ejected in the plume domain. The mass removal mechanism becomes volumetric. Since the plume responds by increasing its pressure and temperature, bubble formation lasts for a very short time. The material pressure adapts immediately to the ambient pressure; the target arrives in a stable liquid state and the material moves towards the binodal again. Here, two effects are observed: since the material heats up, its temperature increases; on the other hand, it tends to adjust itself to the increasing plume pressure. This results in the observed "saw pattern" along the binodal. When the material reaches the critical temperature, oscillations along $T = T_c$ are observed. Above the critical temperature, the material arrives in a supercritical state, where it *fragments*, i.e., a clear liquid-vapor boundary does no longer exist. The supercritical

copper cells quickly enter the plume domain, where they are treated as a dense weakly ionized plasma. The laser will trigger considerable plasma formation in this dense vapor. The plume pressure increases and therefore the target pressure increases as well. Accordingly, the surface cell moves into the region of higher density (at time instant 8.2 ns). Above the surface, the vapor tends to expand. The plume pressure decreases again, driving it towards the critical point. As a result we observe two loops along $T \cong T_c$.

Finally, the plasma above the target becomes so dense, that the material is shielded from the incoming laser light. After 8.2 ns, the surface temperature starts to drop (blue triangles) and the target will follow the right side of the binodal. Hence, in this time frame, condensation of plume material on the target surface starts. In Fig. 5(a), the temporal evolution of the surface temperature and intensity is shown. Fig. 5(b) depicts the pressure ratio over the bubble as well as the ambient pressure P_{amb} versus time. The temporal evolution of the reflectivity at the target surface is shown in Fig. 6(a). Spatial profiles of the density and thermal conductivity in the copper target, at instant 11 ns, are depicted in Fig. 6(b). In the beginning, the laser intensity and surface temperature rise (Figures 5(a) and 6(a)). As a result, the reflectivity starts to drop (Figure 6(a)) and more laser light enters the copper target. The ambient pressure increases rapidly during heating (Figure 5(b)). At 7.9 ns, the pressure ratio drops
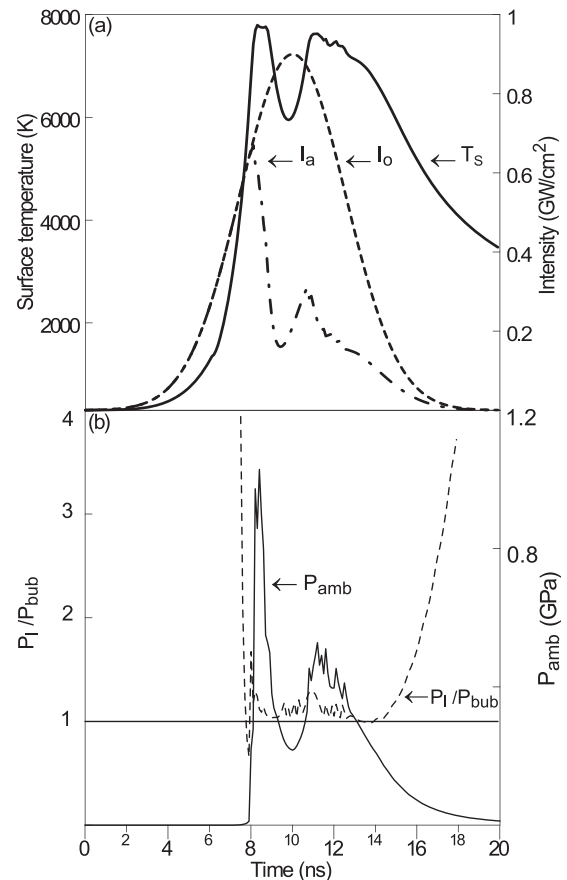

FIG. 5. (a) Temporal profile of original (I_o) and actual (I_a) laser intensities arriving at the target surface as well as the surface temperature T_S. (b) Temporal profile of the pressure ratio across the bubble and the ambient pressure.

below unity and bubble formation starts, immediately followed by an increase in the pressure ratio (see also Eq. (18)); the liquid arrives for a short period in the metastable state and a fast response to the outer pressure drives it again into the stable region (Figure 4). Now the pressure ratio exceeds unity. Between 8.2 and 8.7 ns, a plateau at T_c is observed in Fig. 5(a). Here, two peaks in the ambient pressure profile can be observed from Fig. 5(b). They cause the observed path oscillation around the critical temperature in the phase diagram (Fig. 4). Afterwards, plasma shielding results in a decrease in the laser intensity profile, followed by a decrease in the surface temperature and an increase in the reflectivity (Fig. 6(a)). Above the sample, the pressure starts to drop (Fig. 5(b)), since the vapor expands. As a consequence, the vapor becomes less dense, and plasma absorption becomes less significant. Therefore, the laser light reaches the surface again. Consequently, around 10 ns the temperature and laser intensity profiles increase again (Fig. 5(a)). Since now the temperature stays under T_c, volumetric mass removal cannot proceed. Instead, pressure oscillations are observed, which drive the material towards and away from the binodal. Here, competition between surface evaporation and condensation takes place. Around 11 ns, the surface temperature and the reflectivity reach again a maximum and a minimum value, respectively (Fig. 6(a)). The corresponding spatial profile of the target temperature is depicted in Fig. 6(b). At this instant, the melt front in the material is located at a depth of 0.6 μm; here, a discontinuity in the density ρ and the thermal conductivity κ is observed. Note that these thermophysical properties vary strongly with temperature. This clearly illustrates that the common assumption of constant thermophysical properties is a rather disputable Ansatz.[8,10,12,13,15,16] Around 12 ns, the laser intensity decreases. The material in and above the target responds: the surface temperature and pressure decrease upon thermal cooling, whereas the plume temperature and pressure decrease upon expansion. Since the material cools, the pressure ratio will continue to increase above unity. From that time, condensation of copper on the target surface will dominate the mass transfer between target and plume.

VII. EXPERIMENT

In order to test the model, transmission experiments and ablation depth measurements were carried out. Note that the two experimental measurements are complementary. A transmission study is an indispensable tool for probing the laser energy, distributed between the plasma and the target. In case the transmissivities predicted by the model deviate considerably from the experimental ones, it implies that the model fails to predict the actual energy balance. Since processes that are observed shortly after the laser pulse (such as plume expansion, radiation and nanoparticle formation) are mainly determined by this initial energy distribution, it is unlikely that such a model would succeed in making predictions consistent with the experiment. Therefore, a transmission study should be regarded as a first and fundamental step in model validation. Surprisingly enough, the authors found only a few such studies in the literature.[16,33,63] Since mass removal is governed by the interplay between target and plume, ablation depths can be considered as the final result of a cascade of tightly connected processes. Consequently, ablation depth measurements provide additional valuable information about the ablation process. For the present experiments, a square copper target with an area of 1 cm² is placed in an experimental chamber (stainless steel, 40 cm³) filled with argon at STP. A Nd:YAG laser (Quantel®, YG-981 C Nd:YAG), operating at 532 nm, is focused on the target. In order to ensure a regular, circular laser spot, a circular diaphragm is positioned in the beam path. The resulting laser spot has a diameter of 1.3 mm. Plasma transmission is measured by means of two fast photodetectors (FND-100, rise time < 1 ns), that simultaneously measure the temporal intensity distribution as the laser light enters and leaves the plasma above the target surface. For this purpose, several small holes with a diameter around 15 μm, are drilled in the
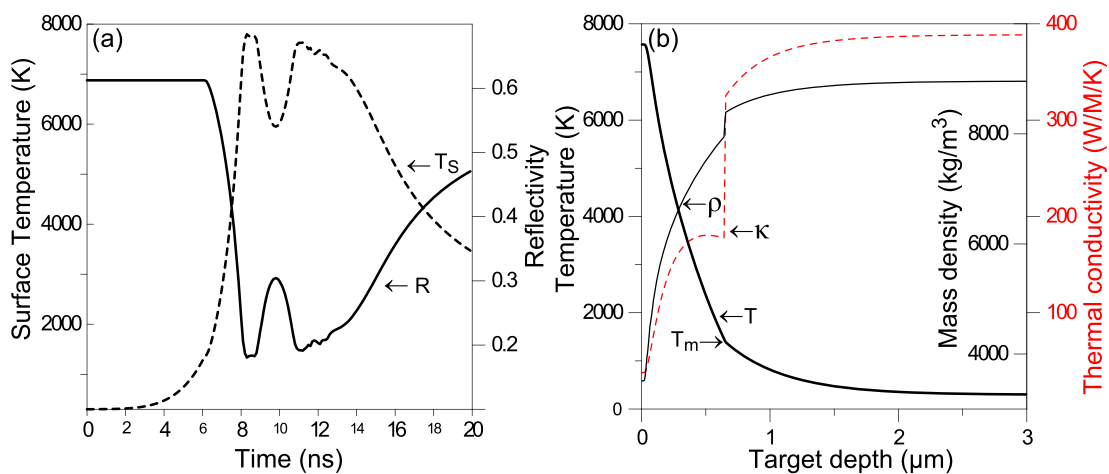

FIG. 6. (a) Temporal evolution of the reflectivity R (solid line) and the surface temperature T_S (dashed). Note that both profile shapes can be mirrored due to the fact that the reflectivity decreases with increasing temperature. (b) Spatial profile of the temperature (black, thick line), mass density ρ (black, thin line), and the thermal conductivity κ (red dashed) at instant 11 ns. Note that the surface temperature acquires its maximum value in the second peak of the bimodal pattern at that instant (see (a)). The discontinuity in the thermal conductivity and mass density can be attributed to the phase change at the melting point T_m.

copper sample. The first photodiode is placed at the beginning of the laser beam path, while the second is placed behind the target. Consecutive single laser shots of 6 ns FWHM, operating in the energy range 0–600 mJ, are fired at different locations on the sample. As the laser light irradiates the sample surface, it can pass through the pre-drilled holes and arrive at the back side of the target. Thus, the actual laser intensity arriving at the sample surface after laser absorption can be measured. The measurement of the ablated depth is performed with a perthometer (Mahr® PGK-120, depth resolution: 5 nm). The instrument consists of a diamond tip that scans the crater surface and surroundings. In a next step, a 3D image of the crater is constructed from the scanned data. Finally, a mean ablation depth, averaged over several laser shots, can be computed from the resulting 3D crater profiles. A detailed description of the entire experimental setup can be found in Ref. 16.

VIII. EXPERIMENTAL COMPARISON

Calculated temporal laser intensity profiles are compared with experimental ones in Fig. 7. Two fluences were chosen, respectively, below and above the one used in Sec. VI (i.e., $F \cong 6 \, \text{J/cm}^2$, $I_{o,max} = 9 \times 10^{12} \, \text{W/m}^2$) and matched with experimental available data. In Fig. 7(a), the applied laser fluence is $F \cong 4.5 \, \text{J/cm}^2$, whereas the intensity profiles for a fluence $F \cong 7.5 \, \text{J/cm}^2$ are depicted in Fig. 7(b). Note that the experimental intensity profiles are slightly shifted compared with the calculated ones. In both cases, the experimental and the calculated intensities I_a, as well as the onset times for laser induced breakdown, $t_{breakdown}$, match reasonably well. At higher fluences, the material can be sustained in the supercritical state for a longer time. In this stage, volumetric mass removal is observed and two competing mechanisms proceed. On one hand the density, temperature, and pressure in the plume will increase during the

influx of target material, resulting in more laser absorption and hence a further increase in pressure, density, and temperature. On the other hand, the plume will tend to expand, resulting in a decrease in density, temperature, and pressure and therefore a decrease in laser absorption. The second peak in the calculated laser intensity profile I_a in Fig. 7(b), as well as its fine structure can be attributed to these competing mechanisms. Note that a similar bimodal pattern was observed in Fig. 5(a). Whether a clear bimodal pattern is observed or not will depend on the exact response of the plume material to variable thermodynamic quantities and consequently on its equation of state. Figures 8(a) and 8(b) show experimental and calculated transmissivities as well as ablation depths, at fluences up to $10 \, \text{J/cm}^2$. The model is now tested for two situations. In the first situation, the target surface cells are constrained to proceed along the binodal during laser heating and moreover the copper target is treated as a transparent medium as soon as it reaches near critical temperatures. As stated above, such a case can be described by surface mechanisms alone: evaporation and condensation (black diamonds). This situation can be referred to as the "evaporation-only case." In the second situation, surface and volumetric mass removal mechanisms are both considered (black crosses). As one can see from Figures 8(a) and 8(b), the experimental results (black circles) deviate considerably from the results for the evaporation-only case. While the experimental breakdown threshold is around $2 \, \text{J/cm}^2$ the evaporation-only case shows a breakdown threshold around $6 \, \text{J/cm}^2$. Moreover, the minimum experimental transmissivity is around 0.36 compared with 0.75 in the evaporation-only case. Since surface evaporation combined with a transparency condition results in limited plasma formation at higher fluences, a significant amount of laser light will reach the target prior to shielding. Indeed, Fig. 8(b) shows a maximum in the calculated ablation depth of $\cong 129 \, \text{nm}$ around $7 \, \text{J/cm}^2$ in the evaporation-only case. A similar profile was observed
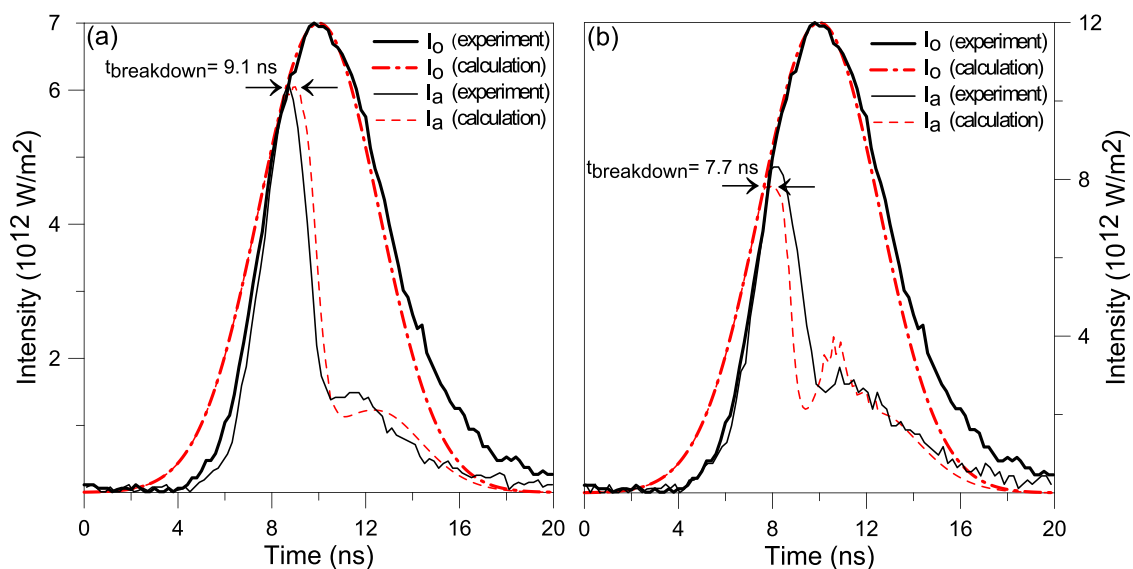

FIG. 7. Temporal profiles of original (I_o) (black, thick solid line) and actual (I_a) (black, thin solid line) measured laser intensities at the copper surface are compared with the corresponding calculated laser intensities (red, dashed-dotted and red, dashed, respectively). The arrows indicate the onset time of laser induced breakdown. Two situations are depicted: (a) $I_{o,max} = 7 \times 10^{12} \, \text{W/m}^2$ ($F \cong 4.5 \, \text{J/cm}^2$) and (b) $I_{o,max} = 12 \times 10^{12} \, \text{W/m}^2$ ($F \cong 7.5 \, \text{J/cm}^2$). The respective calculated onset times of laser induced breakdown are indicated.
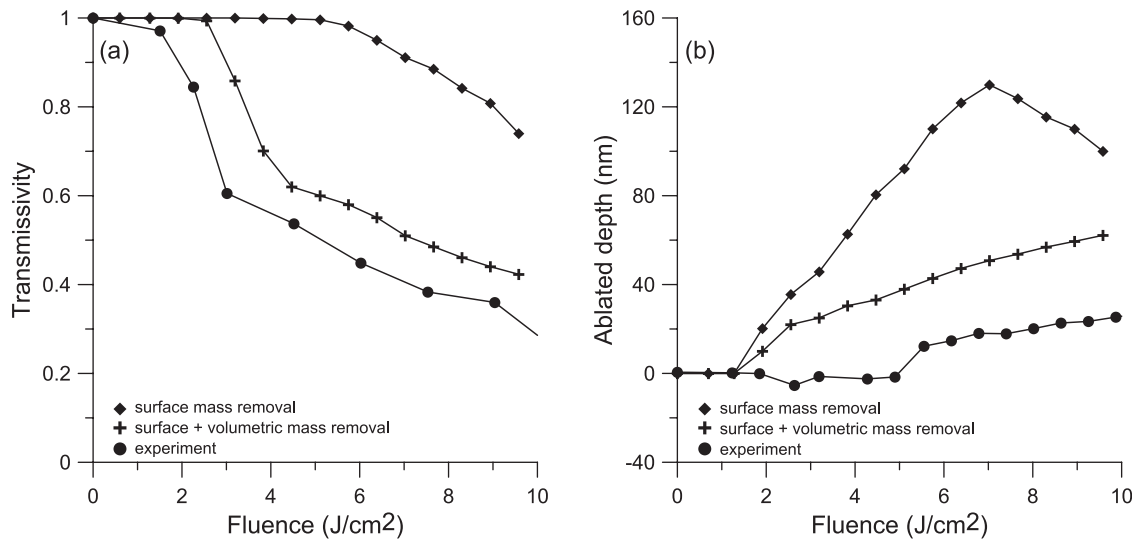
FIG. 8. (a) Comparison of calculated and experimental transmissivities vs fluence. (b) Comparison of calculated and experimentally ablated depths vs fluence. The results of two model settings are shown: considering only surface mechanisms (diamonds), and accounting for both surface and volumetric mass removal (crosses).

in the calculations performed by Clair.[16] However, when both mechanisms are accounted for (black crosses), a reasonable agreement with the experiment is achieved. Here, a breakdown threshold around 3 J/cm^2 and a minimum transmissivity of 0.42 are found. The crater depths scale almost linearly with laser fluence and reach a maximum of 62 nm at 10 J/cm^2.

Finally, it should be emphasized that the calculations in the entire fluence regime revealed that volumetric mass removal due to bubble formation plays a rather minor role in the ablation process. In all cases, the ablation process evolves according to a similar scenario. As soon as the copper target exceeds its normal boiling point, evaporation starts and the pressure above the target increases. When target surface cells enter the metastable liquid phase, they end up in a state *close* to the binodal; here, homogeneous nucleation starts and bubbles grow. Nevertheless, the material resides only for a very short time in the metastable state: as the pressure above the target increases, the copper target responds by increasing its pressure and the material ends up in the stable liquid region. At that instant, bubble formation ends (see also Fig. 4). As laser heating proceeds, the target temperature will rise and surface cells can arrive in the supercritical state. Here, they lose their liquid-vapor interface and they fragment. Hence, volumetric mass removal in the supercritical region starts and a significant amount of target material is removed in a short time. A lot of ablated material ends up in the plume domain and triggers considerable plasma formation, shielding the laser from the target. As a result, the target temperature and pressure decrease, whereas the plume temperature and pressure close to the target increase. In this stage, thermal cooling starts; the copper surface cells follow a trajectory at the right side of the binodal, whereas a significant amount of plume material condenses on the target. Due to the high plasma pressures created above the target, the liquid material evolves all the time in the stable liquid state at the right side of the binodal (see Fig. 4).

Note that the present discussion as well as Figures 4–8 reveals an interesting self-inhibiting mechanism: since volumetric mass removal in the supercritical region triggers plasma shielding, the target temperature decreases below the critical temperature and the mass removal mechanism ends. Hence, the counterintuitive observation can be made that volumetric mass removal does not necessarily result in large ablation depths.

IX. CONCLUSION

In this work, a multiphase model is presented, that accounts for target as well as plume dynamics during pulsed ns-laser irradiation of a copper target. A typical experimental situation as encountered in chemical analysis setups is modelled. The copper sample is placed in argon and irradiated by ns-laser pulses that operate at a wavelength of 532 nm and fluences up to 10 J/cm^2, respectively.

During laser irradiation, a plume consisting of ablated copper expands above the target. In order to probe the distribution of laser energy between the target and the expanding plume, transmission experiments as well as ablation depth measurements were performed and compared with calculated results.

A hydrodynamic model is presented that accounts for surface as well as volumetric mass removal mechanisms. It is demonstrated that plume and target dynamics influence each other strongly; here, the pressure in as well as above the target plays a crucial role in the material evolution. Besides, it is found that bubble formation in the metastable region plays a minor role, whereas material decomposition in the supercritical region acts as the dominant mass removal mechanism. Finally, a self-inhibiting mechanism was observed: since volumetric mass removal in the supercritical region induces plasma screening, the target temperature will decrease below the critical temperature and the decomposition process ends. As a result, the counterintuitive observation

can be made that volumetric mass removal does not necessarily result in large ablation depths. For the present model, a reasonable agreement between the calculated and experimental results was obtained. However, if only surface mass removal mechanisms are considered, a serious deviation between the experimental and calculated results is observed. In this case, a transparency condition is imposed at near-critical temperatures, whereas the target surface cells are constrained to proceed along the binodal during laser heating.

The present findings indicate that a multiphase model is indispensable for the hydrodynamic study of ns-laser ablation.[9,11] Here, the equation of state plays a crucial role since it determines the actual response of the material to variable energy, density and pressure.

ACKNOWLEDGMENTS

[1]D. B. Chrisey and G. Hubler, *Pulsed Laser Deposition of Thin Films* (Wiley, New York, 1994), p. 184.
[2]J. C. Miller and R. F. Haglund, *Laser Ablation and Desorption* (Academic Press, New York, 1998), pp. 15–126.
[3]A. Montaser, *Inductively Coupled Plasma Mass Spectrometry* (Wiley, New York, 1998). pp. 83–224.
[4]R. Singh and J. Narayan, Phys. Rev. B **41**, 8843 (1990).
[5]M. Aden, E. Kreutz, and A. Voss, J. Phys. D: Appl. Phys. **26**, 1545 (1993).
[6]J. R. Ho, C. P. Grigoropoulos, and J. A. C. Humphrey, J. Appl. Phys. **78**, 4696 (1995).
[7]H. Le, D. Zeitoun, J. Parisse, M. Sentis, and W. Marine, Phys. Rev. E **62**, 4152 (2000).
[8]L. Balazs, R. Gijbels, and A. Vertes, Anal. Chem. **63**, 314 (1991).
[9]S. Anisimov and B. Luk'yanchuk, Phys. Usp. **45**, 293 (2002).
[10]A. Bogaerts, Z. Chen, R. Gijbels, and A. Vertes, Spectrochim. Acta, Part B **58**, 1867 (2003).
[11]M. S. Qaisar and G. J. Pert, J. Appl. Phys. **94**, 1468 (2003).
[12]Z. Chen and A. Bogaerts, J. Appl. Phys. **97**, 063305 (2005).
[13]S.-B. Wen, X. Mao, R. Greif, and R. E. Russo, J. Appl. Phys. **101**, 023114 (2007).
[14]V. I. Mazhukin, V. V. Nossov, and I. Smurov, J. Appl. Phys. **101**, 024922 (2007).
[15]M. Aghaei, S. Mehrabian, and S. H. Tavassoli, J. Appl. Phys. **104**, 053303 (2008).
[16]G. Clair and D. L'Hermite, J. Appl. Phys. **110**, 083307 (2011).
[17]F. Garrelie, C. Champeaux, and A. Catherinot, Appl. Phys. A: Mater. Sci. Process. **69**, 45 (1999).
[18]D. Ivanov and L. Zhigilei, Phys. Rev. B **68**, 064114 (2003).
[19]D. Ivanov, B. Rethfeld, G. O'Connor, T. Glynn, A. Volkov, and L. Zhigilei, Appl. Phys. A: Mater. Sci. Process. **92**, 791 (2008).
[20]O. Ellegaard, J. Schou, and H. M. Urbassek, Appl. Phys. A: Mater. Sci. Process. **69**, S577 (1999).
[21]S. Harilal, C. Bindhu, M. Tillack, F. Najmabadi, and A. Gaeris, J. Appl. Phys. **93**, 2380 (2003).

[22]T. Itina, J. Hermann, P. Delaporte, and M. Sentis, Phys. Rev. E **66**, 066406 (2002).
[23]M. Zeifman, B. Garrison, and L. Zhigilei, J. Appl. Phys. **92**, 2181 (2002).
[24]S. I. Anisimov, Sov. Phys. JETP **27**, 182 (1968).
[25]C. J. Knight, AIAA J. **17**, 519 (1979).
[26]A. V. Gusarov and I. Smurov, Phys. Fluids **14**, 4242 (2002).
[27]M. Von Allmen and A. Blatter, *Laser-Beam Interactions With Solid Materials: Physical Principles and Applications*, 2nd updated ed. (Springer Verlag, Berlin, 1995).
[28]D. Bäuerle, *Laser Processing and Chemistry* (Springer Verlag, Berlin, 2011), pp. 201–244.
[29]A. Peterlongo, A. Miotello, and R. Kelly, Phys. Rev. E **50**, 4716 (1994).
[30]A. V. Gusarov and I. Smurov, J. Appl. Phys. **97**, 014307 (2005).
[31]A. Likalter, Phys. Rev. B **53**, 4386 (1996).
[32]V. Batanov, F. Bunkin, A. Prokhorov, and V. Fedorov, Sov. Phys. JETP **36**, 311 (1973).
[33]N. Bulgakova and A. Bulgakov, Appl. Phys. A: Mater. Sci. Process. **73**, 199 (2001).
[34]V. Korobenko, A. Rakhel, A. Savvatimski, and V. Fortov, Phys. Rev. B **71**, 014208 (2005).
[35]J. H. Yoo, S. H. Jeong, R. Greif, and R. E. Russo, J. Appl. Phys. **88**, 1638 (2000).
[36]C. Porneala and D. Willis, Int. J. Heat Mass Transfer **49**, 1928 (2006).
[37]A. Gragossian, S. Tavassoli, and B. Shokri, J. Appl. Phys. **105**, 103304 (2009).
[38]C. Y. Ho, R. Powell, and P. Liley, J. Phys. Chem. Ref. Data **1**, 279 (1972).
[39]S. J. Youn, T. H. Rho, B. I. Min, and K. S. Kim, Phys. Status Solidi B **244**, 1354 (2007).
[40]E. D. Palik, *Handbook of Optical Constants of Solids* (Academic Press, New York, 1997), Vol. 1, p. 280.
[41]B. Chimier, V. Tikhonchuk, and L. Hallo, Appl. Phys. A: Mater. Sci. Process. **92**, 843 (2008).
[42]E. Toro, M. Spruce, and W. Speares, Shock Waves **4**, 25 (1994).
[43]E. Toro, *Riemann Solvers and Numerical Methods for Fluid Dynamics: A Practical Introduction* (Springer Verlag, Berlin, 2009).
[44]P. R. Levashov and K. V. Khishchenko, *Itteos: 5.8 Software for Calculation of EOS for Metals* (Institute for High Energy Densities, Moscow, Russia, 2007), pp. 1-12.
[45]B. Zel'dovich and Y. P. Raizer, *Physics of Shock Waves and High-Temperature Hydrodynamic Phenomena* (Dover, New York, 2002), Vol. 1,2, pp. 192–292.
[46]V. Mazhukin, V. Nossov, M. Nikiforov, and I. Smurov, J. Appl. Phys. **93**, 56 (2003).
[47]V. Morel, A. Bultel, and B. Chéron, Spectrochim. Acta, Part B **65**, 830 (2010).
[48]H. Chung, M. Chen, W. Morgan, Y. Ralchenko, and R. Lee, High Energy Density Phys. **1**, 3 (2005).
[49]A. V. Luikov, T. L. Perelman, and S. I. Anisimov, Int. J. Heat Mass Transfer **14**, 177 (1971).
[50]D. Labuntsov and A. Kryukov, Int. J. Heat Mass Transfer **22**, 989 (1979).
[51]I. I. Beilis, IEEE Trans. Plasma Sci. **13**, 288 (1985).
[52]Y. Sone, S. Takata, and F. Golse, Phys. Fluids **13**, 324 (2001).
[53]M. Keidar, I. D. Boyd, and I. I. Beilis, J. Appl. Phys. **96**, 5420 (2004).
[54]A. Gusarov and K. Aoki, Phys. Plasmas **12**, 083503 (2005).
[55]I. A. Kuznetsova, A. A. Yushkanov, and Y. I. Yalamov, High Temp. **38**, 614 (2000).
[56]V. Mazhukin, V. Nossov, and I. Smurov, Thin Solid Films **453–454**, 353 (2004).
[57]N. Bulgakova, A. Evtushenko, Y. Shukov, S. Kudryashov, and A. Bulgakov, Appl. Surf. Sci. **257**, 10876 (2011).
[58]V. P. Skripov, *Metastable Liquids* (Wiley, New York, 1973), pp. 1–50.
[59]S. Faik, M. Basko, A. Tauschwitz, I. Iosilevskiy, and J. Maruhn, High Energ. Dens. Phys. **8**, 349 (2012).
[60]M. Povarnitsyn, P. Levashov, and K. Khishchenko, Proc. SPIE **7005**, 700508 (2008).
[61]O. Flint, J. Nucl. Mater. **16**, 233 (1965).
[62]V. Carey, *Liquid-Vapor Phase-Change Phenomena* (Hemisphere, New York, 1992), pp. 127–167.
[63]A. Y. Vorob'ev, Sov. J. Quantum Electron. **15**, 490 (1985).